Second Harmonic Generation in Germanium Quantum Wells for Nonlinear Silicon Photonics

ACS Photonics

pubs.acs.org/journal/apchd5

Article

Second Harmonic Generation in Germanium Quantum Wells for Nonlinear Silicon Photonics

Jacopo Frigerio,[‡] Chiara Ciano,[‡] Joel Kuttruff, Andrea Mancini, Andrea Ballabio, Daniel Chrastina, Virginia Falcone, Monica De Seta, Leonetta Baldassarre, Jonas Allerbeck, Daniele Brida, Lunjie Zeng, Eva Olsson, Michele Virgilio,* and Michele Ortolani*

Cite This: https://doi.org/10.1021/acsphotonics.1c01162

Read Online

ACCESS | Metrics & More | Article Recommendations | Supporting Information

ABSTRACT: Second-harmonic generation (SHG) is a direct measure of the strength of second-order nonlinear optical effects, which also include frequency mixing and parametric oscillations. Natural and artificial materials with broken center-of-inversion symmetry in their unit cell display high SHG efficiency, however, the silicon-foundry compatible group IV semiconductors (Si, Ge) are centrosymmetric, thereby preventing full integration of second-order nonlinearity in silicon photonics platforms. Here we demonstrate strong SHG in Ge-rich quantum wells grown on Si wafers. Unlike Si-rich epilayers, Ge-rich epilayers allow for waveguiding on a Si substrate. The symmetry breaking is artificially realized with a pair of asymmetric coupled quantum wells (ACQW), in which three of the quantum-confined states are equidistant in energy, resulting in a double resonance for SHG. Laser spectroscopy experiments demonstrate a giant second-order nonlinearity at mid-infrared pump wavelengths between 9 and 12 μm. Leveraging on the strong intersubband dipoles, the nonlinear susceptibility $\chi^{(2)}$ almost reaches 10^5 pm/V, 4 orders of magnitude larger than bulk nonlinear materials for which, by the Miller's rule, the range of 10 pm/V is the norm.

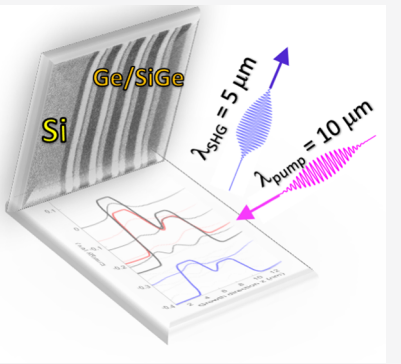

KEYWORDS: *nonlinear optics, germanium, quantum wells, silicon photonics, mid-infrared*

In recent years many research efforts have been devoted to the study and exploitation of nonlinear optical phenomena in silicon photonic integrated circuits (PICs) at infrared (IR) frequencies[1,2] for applications in all-optical signal processing,[3] spectroscopy[4] and quantum optics.[5,6] In this context, second-order nonlinear optics is essential for many classical and quantum applications, from high-speed optical modulation via the Pockels effect[7] to $f-2f$ frequency-comb self-referencing,[8] and even to direct frequency-comb generation by cascaded SHG events that can mimic third-order nonlinear effects.[9] Bulk Si and Ge are compatible with PIC foundry processes,[10,11] however, they feature vanishing second-order susceptibility $\chi^{(2)}$ due to their centrosymmetric unit cell. Several approaches have then been proposed to achieve second-order nonlinearities in silicon PICs: Electric field bias can induce nonlinearity in periodically poled silicon-on-insulator (SOI) waveguides, however, with a rather small $\chi^{(2)}$ = 0.64 pm/V;[12] SHG has been observed in Si_3N_4 waveguides on SiO_x featuring $\chi^{(2)}$ = 2.5 pm/V,[13] and more recently in microresonators.[14] The transparency range of both SOI and Si_3N_4 waveguides is, however, limited to wavelengths $\lambda < 4$ μm as a result of the strong phonon absorption of SiO_x.[15−17] Proposed unconventional approaches to generate optical nonlinearity in bulk Si include nanostructures with strain gradients,[18] which are difficult to realize in a controlled manner, multiphoton absorption by impurities in Si,[19−21] which is, however, limited to the far-IR, and nonlinear free-electron plasma oscillations in heavily doped Si or Ge,[22] which are accompanied by high ohmic losses. A different solution for second-order nonlinearity in Si PICs is here provided by asymmetric-coupled quantum wells (ACQWs) made of SiGe epitaxial layers grown on Si substrates (Figure 1a). ACQWs are a type of semiconductor heterostructure based on two quantum wells of different thicknesses and/or compositions, separated by a thin tunneling barrier (Figure 1b). Electrons or holes confined into the ACQW planes (the epitaxial growth direction being normal to those planes) populate quantized levels arranged in discrete subbands, that is, "copies" of either the valence or the conduction band separated by the differences in quantization energy E_i (Figure 1c). In ACQWs, either holes or electrons provide the dipole strength for the nonlinear interaction of the material with the laser pump through their intersubband transitions (ISBTs).[23,24] The ACQW subband structure can be specifically designed for resonant enhancement of certain

Received: July 31, 2021

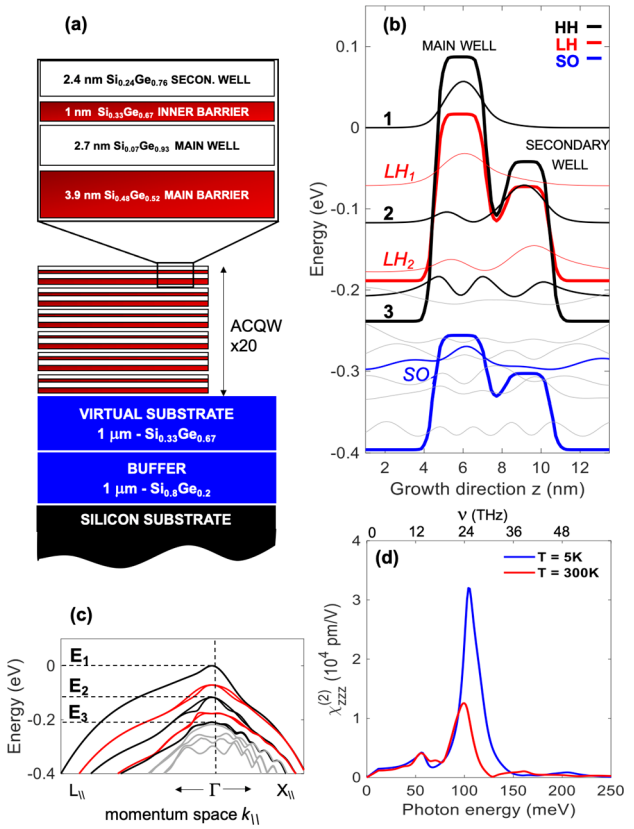

Figure 1. (a) Schematic of sample A showing the different epitaxial block thickness and composition: buffer, virtual substrate, and ACQW stack repeated 20 times. (b) Valence band-edge profiles of sample A forming the main and secondary wells (thick lines, HH: heavy holes; LH: light holes; SO: split-off band) and the subband wave functions (thin lines; for holes, wells correspond to band-edge potential maxima and transitions are downward in energy). (c) In-plane dispersion of the hole states in the first Brillouin zone around the Γ point as a function of the in-plane wavevector $k_{||}$. (d) Calculated second-order nonlinear susceptibility $\chi^{(2)}_{zzz}$ for one single heterostructure period as a function of the pump photon energy and frequency. Impurity transitions are not included in our model.

nonlinear effects (here, SHG) and they can behave as artificial nonlinear materials with high efficiency.[25−27] It is important to notice that the ACQW second-order nonlinearity is purely based on the electron wave functions being asymmetrically delocalized in the two coupled wells and not on the crystal lattice asymmetry, as in natural nonlinear materials. Then, the Miller's rule, a phenomenological argument for estimating nonlinear susceptibilities based on the value of the crystal lattice parameter does not hold for ACQWs,[23,24] releasing the physical limit setting the value of $\chi^{(2)}$ in the range of 10 pm/V for all existing natural nonlinear crystals.[5] One can then quantum-design the ACQW wave functions and obtain a giant $\chi^{(2)}$ for SHG up to 10^5 pm/V,[25−28] exploiting the key fact that, in an ideal ISBT, the joint optical density of states is a Dirac delta function, because all initial and final subband states have exactly the same energy distance, unlike in a conventional interband transition. The design criterion for SHG in ACQWs is that the ISBT energies $h\nu_{12}$ and $h\nu_{23}$ (where $h\nu_{ij}$ is the energy of the ISBT between i and j, hereafter indicated as $i \rightarrow j$) should both be in resonance with the pump photon energy $h\nu_{pump}$ or $h\nu_{12} \cong h\nu_{23} \cong h\nu_{pump}$. Setting the z axis parallel to the carrier confinement direction (i.e., orthogonal to the QW growth plane), the $\chi^{(2)}_{zzz}(2\nu)$ element of the second-order susceptibility tensor can be conveniently approximated, assuming parabolic subband dispersion, by the following expression:[23]

$$\chi^{(2)}_{zzz}(2\nu) = \frac{q^3(N_1 - N_2)}{\epsilon_0 h^2} \frac{z_{12}z_{23}z_{31}}{(\nu - \nu_{12} - i\gamma)(2\nu - \nu_{13} - i\gamma)} \quad (1)$$

where N_i is the 3D population density of subband i, z_{ij} is the vertically oriented dipole moments of $i \rightarrow j$, and g is the intrinsic line width assumed identical for all ISBTs. N_i is calculated as the 2D free carrier density divided by the total ACQW heterostructure period. In symmetric systems where parity is a good quantum number, $z_{31} = 0$ because z is an odd operator, and therefore, SHG is forbidden according to eq 1. This selection rule is broken for asymmetric systems like ACQWs.[23,24] In the ideal case of parabolic subband dispersion, ν_{ij} does not depend on the in-plane crystal momentum $k_{||}$ and the SHG doubly resonant condition is obtained at the same ν_{pump} for all electrons (or holes) populating the involved subbands, while in real cases one has to integrate over $k_{||}$ in the entire 2D Brillouin zone and the SHG resonance spectrum can broaden considerably.[28] Not only the ACQW structure breaks the inversion symmetry as required for SHG, but it also provides the freedom of wave function design to achieve doubly resonant second-order electromagnetic interaction.[24] In addition, the doping level sets the strength of the nonlinearity. The doping can be introduced by chemical substitution (in this work B for Ge and Si) or it can be modulated at the picosecond time scale with a near-IR optical pump.[29]

SHG has been systematically observed in the mid-IR from ACQWs[23,25,26] made of III−V compound semiconductor materials and, in a pioneering work, also from Si-rich SiGe ACQWs.[30] Attempts to reach PIC-standard wavelengths in the near-IR with intersubband transitions have been done using high band offset semiconductor pairs[31] and metal−dielectric heterostructures.[32] Recently, SHG efficiency enhancements of 3 orders of magnitude have been reported in III−V compound ACQWs using plasmonic nanoantennas[26,33] and diffraction grating couplers[27] for electric field enhancement; however, the integration of ACQW nonlinearity into silicon PICs has never been targeted before. In this work, we demonstrate SHG in Ge-rich SiGe ACQWs grown on Si substrates (as shown in Figure 1a) using silicon-foundry-compatible processes. The epitaxial deposition of Ge-rich SiGe heterostructures on silicon has undergone an impressive development in the past decade driven by the envisioned applications in telecom and datacom. Optical modulators based on Ge/SiGe multiple quantum wells have been reported[34−36] and Ge/SiGe quantum cascade lasers are under investigation.[37,38] In the case of nonlinear PICs, the use of Ge-rich heterostructures will be necessary to realize integrated rib or ridge waveguides, which is a requirement to obtain long interaction regions for efficient SHG in PICs without having to use very high pump power densities. Indeed, Ge/SiGe epitaxial layers forming the ACQWs (refractive index n close to 4.0) can be etched to form the waveguide core on top of the Si substrate (n = 3.4), operating as the waveguide cladding together with the air or the dielectric environment, an ideal configuration for on-chip mid-IR spectroscopy applications.[39−42]

The interband transition edge of Ge in the near-IR at 0.66 eV together with its high transparency region extending to $\lambda <$

https://doi.org/10.1021/acsphotonics.1c01162
ACS Photonics XXXX, XXX, XXX−XXX

Table 1. Summary of Design and Measured Parameters of the Four Samples

sample	wave function design	main well thickness t_w (nm)	acceptor density N_a (cm^{-2})	measured hole density N_{tot} (cm^{-2})	measured SHG efficiency K_2 (1/W)
A	doubly resonant	2.7	4.2×10^{11}	$(3.9 \pm 0.3) \times 10^{11}$	5.7×10^{-3} ($\pm 1.1 \times 10^{-3}$)
B	doubly resonant	2.7	2.1×10^{11}	$(2.5 \pm 0.3) \times 10^{11}$	1.4×10^{-3} ($\pm 0.3 \times 10^{-3}$)
C	single resonance	3.0	4.2×10^{11}	$(3.9 \pm 0.3) \times 10^{11}$	0.6×10^{-3} ($\pm 0.1 \times 10^{-3}$)
D	reference	2.7	undoped		$<0.1 \times 10^{-3}$

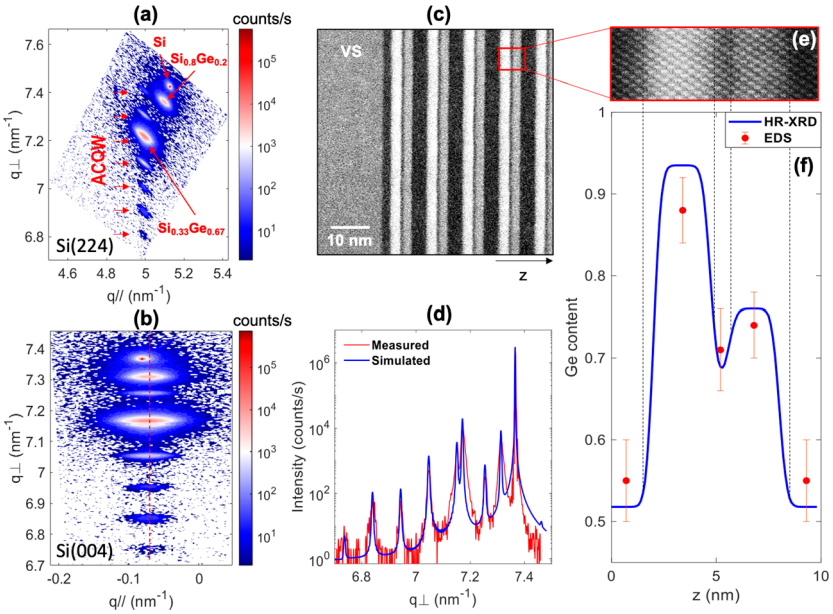

Figure 2. (a, b) HR-XRD reciprocal space maps of sample A with respect to the (224) and (004) Si reflections. (c) STEM images of a different piece of sample A. (d) ω–2θ scan of the Si(004) reflection (red) together with Darwin model simulations (blue) performed to extract the Ge composition of each layer and the intermixing depth. (e) High-resolution STEM, greyscale intensity is proportional to local Ge content. (f) Ge content profile of sample A retrieved from HR-XRD measurements (blue curve) and by EDS measurements (red dots).

15 μm, make it the ideal material for mid-IR PICs, whereas intrinsic absorption losses limit waveguiding in pure Si to $\lambda < 8$ μm.[43−45] Here, we aimed at demonstrating the nonlinear Ge/SiGe ACQW operation in a broad mid-IR wavelength range: laser pump wavelengths were selected in the 12 to 9.2 μm range (SHG wavelengths from 6.0 down to 4.6 μm). We leverage on hole-doped rather than electron-doped structures in order to exploit the larger valence band offsets up to 0.5 eV. It is worth noticing that ISBTs in hole-doped materials, at odds with more common electron-doped ACQWs, also feature nonvanishing in-plane components of the optical transition dipoles connecting the heavy hole (HH), light hole (LH), and split-off (SO) valence bands. Consequently, one could achieve also large off-diagonal tensor components $\chi^{(2)}_{xzl}(2\nu)$ with $l = x$, y, or z thus opening interesting opportunities to realize polarization mixing in nonlinear phenomena.[46,28] In this work, however, we have designed and investigated samples with an epitaxial structure specifically optimized for SHG featuring three energy levels E_1, E_2, and E_3 belonging to the HH band (**well**/barrier thickness **2.4**/1.0/**2.7**/3.9 nm, and Ge content x_{Ge} = **0.76**/0.67/**0.93**/0.52, see Figure 1). The levels are equally spaced: $h\nu_{12} = h\nu_{23}$. Sample design parameters are reported in Table 1: if compared to the ideal case of sample A, sample B has half the doping level, sample C has its E_3 purposely offset from double SHG resonance ($h\nu_{12} \neq h\nu_{23}$), which was obtained by varying the main well width only, and sample D is undoped. Samples B−D are used for comparison to define the performance of the ideal sample A, whose predicted $\chi^{(2)}_{zzz}(2\nu)$ is reported in Figure 1d (other tensor components $\chi^{(2)}_{zjk}(2\nu)$ are reported in Supporting Information, a).

EXPERIMENTAL RESULTS

The samples have been grown by low-energy plasma-enhanced chemical vapor deposition (LEPE-CVD)[47] on Si(001) wafers, a standard for PICs (see Supporting Information, b). The superlattice consists of 20 periods of the ACQW stack shown in Figure 1a. Such low number of ACQW repetitions has been chosen to optimize the linear dichroism effect of ISBTs in IR transmission spectroscopy,[38] but it should be pointed out that the growth procedure can be straightforwardly extended to deposit hundreds of ACQW periods[48] required to fill the ridge height >2 μm of a mid-IR integrated waveguide[43]

A Si-rich buffer layer is deposited at the interface with the Si substrate to reduce the lattice mismatch (hence, the threading dislocation formation at the initial stage of the relaxation).[49] A Ge-rich layer is then deposited to serve as a virtual substrate for the growth of ACQWs. High resolution X-ray diffraction (HR-XRD) has been used to measure the Ge content, the strain and the in-plane lattice parameters for all samples. A clear superlattice period is observed indicating regular periodicity of the ACQW structure (Figure 2a,b, see Methods). The scanning transmission electron microscopy (STEM) image in Figure 2c,e shows ACQWs with sharp interfaces arranged in identical subsequent periods along the growth direction z. The corresponding energy-dispersive X-ray emission spectroscopy

https://doi.org/10.1021/acsphotonics.1c01162
ACS Photonics XXXX, XXX, XXX−XXX

(EDS) data (red marks in Figure 2f) confirm the different Ge content in the two wells obtained by fitting the HR-XRD data (blue curve in Figure 2f), which is crucial to break the inversion symmetry for SHG.

Ge/SiGe heterostructures with narrow wells, abrupt interfaces and high compositional mismatches between adjacent layers pose significant challenges in terms of epitaxial deposition. To this aim, one has to consider that, unlike III−V semiconductors, Si and Ge are completely miscible over the entire compositional range. As a consequence, the realization of atomically sharp interfaces is hindered by entropic intermixing of Si into pure Ge layers and Ge into SiGe layers. Therefore, the pure Ge/SiGe heterostructures proposed in ref 28 could not be grown, because the actual compositional profile is smoothed out by intermixing and, in the case of the main well, also by the presence of residual SiH_4 gas in the CVD reactor. The resulting ACQW potential profile of sample A shown in Figure 1b represents the best possible compromise, with $h\nu_{12} = h\nu_{23} = 105$ meV and a doubly resonant giant $\chi^{(2)}_{zzz}$ up to 3×10^4 pm/V, as seen in the calculation of Figure 1d, in which the subband energy separation dependence on $k_{\parallel}$ has been taken into account in order to compute $\chi^{(2)}_{zzz}$ (2ν) by integrating over the crystal momentum in the entire 2D Brillouin zone. Although the pure Ge/SiGe heterostructure design proposed in ref 28 had $h\nu_{12} = h\nu_{23} = 120$ meV and $\chi^{(2)}_{zzz}$ up to 1×10^5 pm/V,[28] the presently expected values of $\chi^{(2)}_{zzz}$ are still 3 orders of magnitude higher than those of typical nonlinear crystals; however, the total SHG emitted power can be comparable because the interaction length in bulk crystals can be generally made longer than it is in heterostructures and absorption losses are generally much lower.

The linear absorption by ISBTs in the doped samples A, B, and C was measured by Fourier Transform Infrared spectroscopy (FTIR) in linear dichroism mode to filter out the substrate contributions, with the samples prepared in the prism-shaped slab-waveguide configuration, as sketched in Figure 3a, where the TM polarization senses the ISBTs with a dipole along z and the TE polarization is used for an internal reference. In the dichroic absorption spectra of Figure 3b,d, one can observe that all samples display two ISBT peaks of similar intensity: the low frequency peak around 32 THz is naturally assigned to 1 → 2, and the high frequency peak (58 THz in samples A and B and 53 THz in C) to 1 → 3. Note that sample C was intentionally detuned by design from the double resonance condition, but also in samples A and B the perfect double resonance condition $h\nu_{13} = 2h\nu_{12}$ is only approximately realized. The best-fit Lorentzian frequencies ν_{ij}, oscillator strengths f_{ij}, and half-line widths γ_{ij} of the absorption peaks are reported in Supporting Information, c.

The main effect of heating the samples to 300 K is the notable broadening of the ISBT line widths, as shown in Figure 3d. At room temperature, due to thermal excitation, carriers are spread in the k space around the Γ point, hence, the nonparabolicity of the subbands produces a nontrivial dependence of the ν_{ij} values on $k_{\parallel}$, which is the main factor contributing to the broadening of the line widths. This effect is also responsible for the temperature-induced redshift of the 1 → 3 absorption peak. In fact, the population of the fundamental subband at larger $k_{\parallel}$ due to thermal excitation activates different 1 → 3 transitions featuring lower photon energies, as it can be argued from the nonparabolicity of the band structure shown in Figure 1c. Intrinsic line broadening effects at finite-T are expected to constitute the main limitation

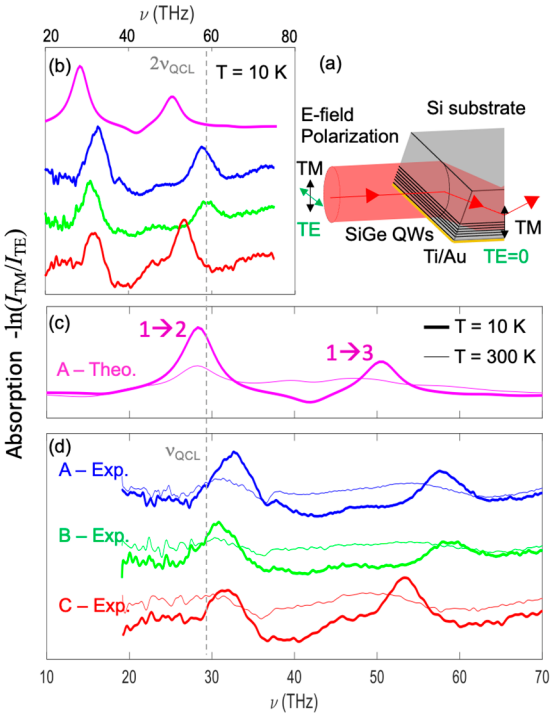

Figure 3. Linear dichroic absorption spectroscopy of the doped ACQW samples A, B, and C. (a) Sketch of the surface-plasmon waveguide structure with prism-shaped slab geometry. The electric field polarization in the illuminated ACQW region is mostly vertical (TM-mode transmitted intensity I_{TM}), while the TE-mode transmitted intensity I_{TE} serves as spectral reference. (b) Dichroic absorption $-\ln(I_{TM}/I_{TE})$ from the theoretical model of sample A (magenta curve, the main ISBT transitions are marked) and from the experiments at $T = 10$ K. (c, d) Enlarged view of the curves in panel b at $T = 10$ K (thick lines). Data at $T = 300$ K are also reported (thin lines). Note that the horizontal scale of panels c,d is exactly double of that of panel b to highlight SHG resonance in samples A and B. The vertical dashed gray line marks the QCL pump frequency of 29.3 THz in panels c and d and its double (58.6 THz) in panel b. The QCL pump photon energy is 120 meV to compare with Figure 1d.

to the SHG power that can be obtained from doubly resonant ACQWs.

In Figure 3b,d, the experimental spectra are plotted on two different horizontal scales to highlight SHG resonances, with an indication of the selected pump photon frequency for the experiments described below employing a quantum cascade laser (QCL) pump (samples cooled to 10 K).One can identify by comparing Figure 3b and d, the perfect resonance of $2\nu_{QCL}$ = 58.6 THz with ν_{13} of samples A and B. Lastly, we compare in Figure 3c,d the theoretical and experimental dichroic absorption spectra for sample A. The overall spectral shape and the absorption intensities are very well reproduced by our calculations at both T values. The dip at 40 THz is a signature of the TE-polarized ISBT 1 → LH_2, in good agreement with the energy difference of 175 meV observed in Figure 1b. The rigid frequency offset of approximately 7 THz for the two TM-polarized peaks 1 → 2 and 1 → 3 can instead be attributed to the many-body depolarization effect, not included in our calculations (see Methods), which induces a blueshift of the TM-polarized absorption frequencies if compared to the bare bandstructure energy differences in Figure 1b. Note that the values to be inserted in eq 1 are the actual absorption frequencies, not the bare energy differences.

https://doi.org/10.1021/acsphotonics.1c01162
ACS Photonics XXXX, XXX, XXX−XXX

The demonstration of the doubly resonant nonlinearity in Ge/SiGe ACQWs is here provided by experimental comparison of samples A and C at 10 K with different ν_{13} but otherwise identical relevant parameters: ν_{12}, doping, and number of periods. We used ν_{QCL} = 29.3 THz ≈ $\nu_{13}/2$ for sample A; however, there is a slight detuning $\Delta = \nu_{12} - \nu_{QCL}$ that reduces the pump intensity depletion while traveling through the waveguide: this choice of ν_{QCL} maximizes the SHG efficiency difference between samples A and C and also the total SHG intensity, as we shall see below.

The experimental setup is sketched in Figure 4a (the waveguide length crossed by the pump radiation beam is approximately 400 μm long, see Methods for details). Using a calculated spot size of 1.3 × 10^{-3} cm^{-2}, we estimate a peak power density at focus for the nonattenuated pump $I_{QCL,max}$ = 23 W/cm^2 (see Supporting Information, d). The resulting emitted SHG power P_{SHG} is plotted in Figure 4b as a function of I_{QCL}: a square-law relation is fitted to the integrated power data set $P_{SHG} = K_2 P_{QCL}^2$ (see Supporting Information, e). The value of K_2 in W^{1-} reported in Table 1 is a measure of the SHG generation efficiency, because it is proportional to the square of $\chi^{(2)}_{zzz}(\nu)$ calculated at ν_{pump} = 29.3 THz. The resonance of $2\nu_{pump}$ with 1 → 3 of sample A then explains its highest K_2. Sample B is also resonant at 1 → 3, but its doping level is almost half of that of sample A, and therefore, its K_2 is approximately 4× lower than that of sample A. Finally, sample C, in spite of the same doping level as sample A, has the lowest K_2, apparently because it is not doubly resonant. This interpretation is supported by calculations based on eq 1 (see Supporting Information, d). We note that a maximum dimensionless conversion efficiency P_{SHG}/P_{QCL} = 1.5 × 10^{-4} at $I_{QCL,max}$ = 23 W/cm^2 in sample A is comparable to that found in recent experiments performed with a similar QCL pump on InGaAs/AlInAs ACQWs with comparable number of periods.[26,27]

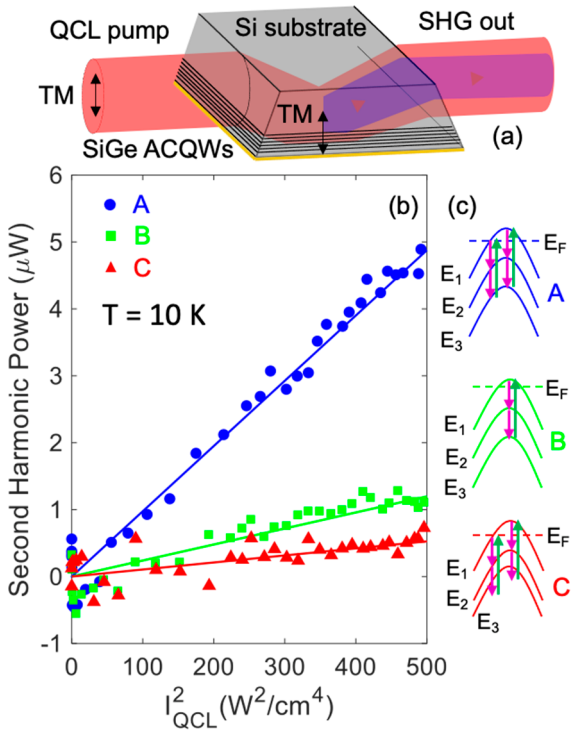

Figure 4. (a) Scheme of the nonlinear experiment for absolute characterization of SHG efficiency. In the TM mode, the radiation electric field is oriented along the ISBT dipoles of the resonant HH transitions. (b) Measured SHG power vs squared pump power density at focus for samples A, B, and C. Sample D was used as reference to subtract the linear background. Also, the SHG emission disappeared when the sample was shifted by ±1 mm (twice the estimated depth of focus) because the electric field value dropped quickly when the ACQWs were out of focus. This technique was used to subtract the contribution of the residual pump photons to the detector signal. (c) Simplified sketch of the SHG process in the HH valence band. E_F: Fermi level. Note that hole ISBTs 1 → 2 and 2 → 3 are represented by downward arrows.

In order to clearly demonstrate nonlinear emission at room temperature, we pumped the samples with very high peak-power pulses from a nonlinear optical parametric amplifier (NOPA) driving a difference-frequency generation (DFG) setup in Figure 5a.[50] The maximum power density at focus inside the sample I_{DFG} = 9 × 10^7 W/cm^2 is more than 6 orders of magnitude higher than that of the QCL pump. The tunability and the high power of this optical pump permit the investigation of SHG efficiency in the entire frequency range, where eq 1 provides significant values and not only at the peak value, as for the QCL pump. In particular, we used the three DFG pulses in Figure 5b,c with center frequency $\nu_{DFG,1}$ = 25 THz (ν_{pump} slightly off resonance), $\nu_{DFG,2}$ = 29 THz ($2\nu_{pump}$ at resonance with ν_{13}), and $\nu_{DFG,3}$ = 32 THz (ν_{pump} at resonance with ν_{12}).

In waveguides containing ACQWs, when pumping at resonance with ν_{12}, the pump intensity is rapidly depleted, ending up in an interaction region shorter than the waveguide length. Therefore, in ACQWs it is generally convenient to pump in exact resonance with $\nu_{13}/2$, instead. This scenario is approximately confirmed by the SHG spectra for sample A: the red dashed line in Figure 5d represents the $\chi^{(2)}_{zzz}$ calculation based on eq 1 (not accounting for pump depletion) using the data of Figure 3 (see Supporting Information, c). This calculation predicts approximately equal SHG efficiencies for $\nu_{DFG,1}$ and $\nu_{DFG,3}$, however, the SHG efficiency observed in Figure 5d with the pump tuned at $\nu_{DFG,3}$ is 3× lower than at $\nu_{DFG,1}$.

The shaded gray Lorentzian curve represents the effect of the 1 → 2 ISBT in depleting the pump beam, which is obviously stronger at $\nu_{DFG,3}$; one can also see that even at $\nu_{DFG,2}$ the ideal SHG efficiency is not reached due to pump depletion. We note that, at these very high pump intensities, 1 → 2 absorption saturation and free carrier heating (i.e., high-$k_{||}$ states occupied by holes in the subband 1, leading to broader effective transition line widths) can also play a role in decreasing the observed SHG efficiency from the ideal value.

Finally, in Figure 5e, the relative efficiency of samples A, B, and C when pumping at $\nu_{DFG,2} \approx \nu_{QCL}$ compares very well with that of Figure 4b: sample B is less efficient than sample A, due to lower doping levels, and sample C because it is not doubly resonant. No SHG emission was observed from the undoped sample D.

DISCUSSION

In Figure 6 we plot, for sample A, the emitted SHG peak power versus the peak pump power for both QCL and DFG pumps, in a log–log scale. It can be seen that the slope of the QCL data, corresponding to a quadratic dependence on the input pump power density, is not maintained in the DFG pump power range. An almost linear dependence is observed

https://doi.org/10.1021/acsphotonics.1c01162
ACS Photonics XXXX, XXX, XXX−XXX

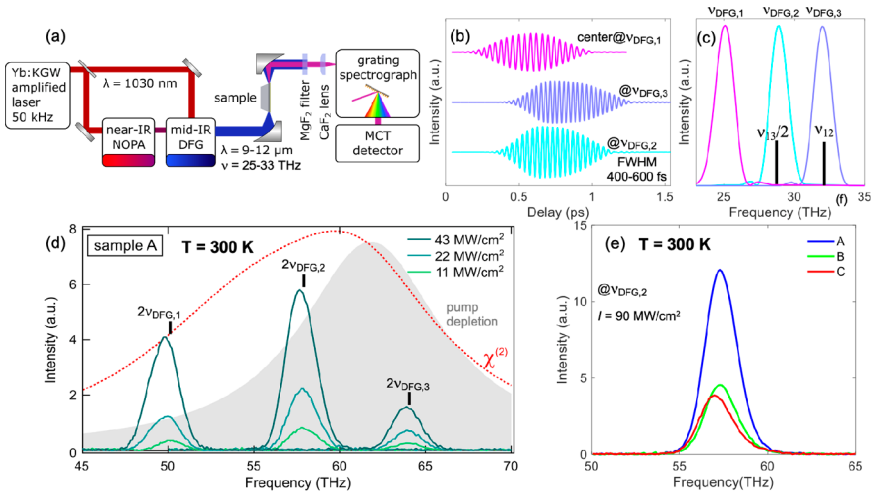

Figure 5. SHG performance with high-intensity ultrashort pulses. (a) Experimental setup based on difference-frequency generation (DFG) and spectrally resolved detection with a mercury−cadmium telluride (MCT) diode. (b, c) Field-time profiles obtained by electro-optic sampling and corresponding FT spectrum of MIR pump pulses employed in the experiment. (d) SHG spectra measured with sample A at different pump frequency and intensity. (e) SHG efficiency of different samples at optimal pumping conditions (i.e., $\nu_{DFG,2}$ and highest pulse power).

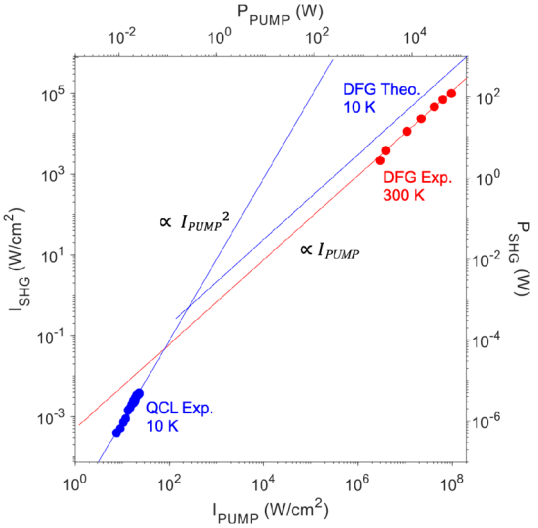

Figure 6. Log−log plot of SHG emission power vs pump power density for all QCL and DFG pump experiments performed on sample A. A quadratic slope has been superimposed to the QCL data, and a linear slope to the DFG data. Note that the two experiments have been performed at different sample temperatures. The theoretical DFG line at 10 K is drawn parallel to the 300 K derived from the efficiency improvement, with cooling predicted in Figure 1d.

instead, a fact that we relate to a concurring two-photon absorption (TPA) effect that, at very high pump intensities, becomes a non-negligible competitor of the SHG process.[5] Indeed the presence of the 1 → 3 ISBT at twice the pump frequency makes the TPA effect non-negligible at high pump intensities. In quantum well systems displaying ISBTs, the radiative decay of the excited states (photoluminescence) is negligible if compared to the nonradiative decay; therefore, the emission spectrum only shows SHG. The competition between TPA and SHG sets an ultimate high pump-power limit to SHG efficiency in SiGe ACQWs. The expected transition between a quadratic regime at low pump power to a linear regime at high pump power can be inferred by plotting in Figure 6 a line parallel to the 300 K best-fit line considering the SHG efficiency improvement at 10 K shown in Figure 1d.

The experimental value of $\chi^{(2)}$ to be compared with calculations should then be extracted from the QCL pump experiment using the definition of $\chi^{(2)} = F_{2w}/F_w^2$, with F being the electric field intensity at focus. Using K_2 of sample A from Table 1 we find $\chi^{(2),exp} = 5 \times 10^4$ pm/V for one single heterostructure period (see Supporting Information, d). This value compares well with the predicted peak value at 10 K of $\chi^{(2),theo} = 3 \times 10^4$ pm/V (see Figure 1d), the disagreement being probably related to uncertainty in the detector calibration. Notice that in ACQWs the giant $\chi^{(2)}$ is counterbalanced by high propagation losses due to strong absorption of both the pump and the SHG signal by the resonant ISBTs.[23−25]

A final consideration is worth phase matching. In nonlinear crystals, the difference in the phase velocity $c/n(\nu)$ between pump and second-harmonic defines a maximum length along the waveguide over which the SHG power adds up coherently to that generated in previous positions along the waveguide, thereby imposing an upper limit to the SHG efficiency. In III−V compound semiconductor ACQWs at mid-IR frequencies, the dispersion due to the strong polar optical phonon absorption at around 10 THz limits SHG phase coherence. Instead, in SiGe ACQWs, which feature a nonpolar crystal lattice, the dispersion due to phonons is totally absent. In integrated waveguides, the modes will still have a dispersion due to the varying ratio between λ and the (fixed) geometrical parameters of the waveguides, but in the presently employed slab waveguide, this source of dispersion is negligible. There also exists a residual dispersion generated by the ISBT absorption resonances themselves, but this phenomenon can be neglected in the case of detuning from exact resonances, as for example when pumping the sample A at 25 and 29 THz. Therefore, in most of the present experiments, homogeneous phase matching conditions apply, without having to include specific dispersion−compensation structures. This also indicates that there is considerable room for improvement of the observed SHG power levels by pumping through properly fabricated SiGe ridge waveguides with millimeter-scale lengths.

https://doi.org/10.1021/acsphotonics.1c01162
ACS Photonics XXXX, XXX, XXX−XXX

CONCLUSION

We have designed, grown, and optically analyzed hole-doped Ge/SiGe asymmetric-coupled quantum wells optimized for second harmonic generation in silicon photonic chips. A giant second-order nonlinearity, 4 orders of magnitude higher than that of any natural nonlinear material, is observed with laser pump wavelengths in the 9.2 to 12 μm range (second harmonic in the 4.6 to 6 μm range), well within the even broader transparency range of existing Ge-rich integrated waveguides that have been developed for on-chip spectroscopic sensing applications. The giant nonlinearity is attributed to the double-resonance effect of the laser pump photon energy and the SHG photon energy with the intersubband transitions among three confined energy levels equally spaced in energy. The absolute nonlinear susceptibility has been determined at low temperatures and found to be in good agreement with wave function calculations. Room-temperature operation with ultrashort pulses has shown that the optimal SHG efficiency is obtained for small red-detuning of the pump photon energy from the double resonance. The material growth technology and the infrared wavelength range employed here are compatible with the standard silicon photonics foundry processes, opening the way to the on-chip integration of second-order optical nonlinearities, to be exploited in future molecular sensing and free-space telecommunication devices.

METHODS

Theoretical Calculations. The valence band structure has been calculated relying on a semiempirical tight-binding Hamiltonian model in the first neighbor approximation.[51,52] The adopted basis set includes $sp^3d^5\sigma^*$ orbitals in both spin configurations. Self and hopping energies together with scaling exponents used to account for the strain-induced lattice distortion are reported in refs 53 and 54 for Si and Ge, respectively. In order to properly describe nonparabolicity effects, the linear absorption and second harmonic susceptivity spectra have been calculated performing a 3D sampling of the BZ zone in a neighbor of the G point. Dipole matrix elements have been estimated following the procedure given in ref 51. $\chi^{(2)}_{lmn}(2\nu)$ has been calculated assuming that holes populate the fundamental subband only following eq 1 of ref 28, which describes both resonant and nonresonant contributions. A Lorentzian line shape with a HWHM of 5 meV has been used to phenomenologically describe the line broadening of the ISBTs.

Sample Growth and Characterization. Samples A–D were grown by low energy plasma-enhanced chemical vapor deposition (LEPECVD)[47] on a 100 mm intrinsic Si(001) substrates with a resistivity >6000 Ω·cm. Before heteroepitaxy, the native oxide was removed by dipping the substrate in aqueous HF solution (HF:H_2O 1:10) for 30 s. The first part of the structure consists of a 1 μm thick $Si_{0.8}Ge_{0.2}$ layer deposited at a rate of 5 nm/s at a temperature of 600 °C. The deposition was followed by an in situ thermal annealing at 700 °C for 30 min in order to promote the full relaxation of the layer. The second part of the structure consists of a 1 μm thick $Si_{0.3}Ge_{0.7}$ deposited at 5 nm/s at 500 °C forming a fully relaxed virtual substrate for the ACQW stack. The ACQW structure has been grown at a rate ∼0.1 nm/s at a temperature of 350 °C to minimize the intermixing, and it consists of 20 repetitions of the following sequence: $Si_{0.1}Ge_{0.9}$ main well/$Si_{0.4}Ge_{0.6}$ tunneling barrier/$Si_{0.25}Ge_{0.75}$ secondary well/$Si_{0.4}Ge_{0.6}$ main barrier. The main well has been p-doped in situ by adding B_2H_6 during the growth. The thickness of the main barrier has been designed to obtain a mean Ge concentration in the ACQW stack equal to the one of the VS. In this way the compressive strain of the wells is compensated by the tensile strain in the barriers, thus, obtaining a strain-symmetrized structure.

A XRD apparatus was used to record the (224) and (004) reciprocal space maps of sample A are shown in Figure 2a and b, respectively. Figure 2c shows the (004) ω–2θ scan of Sample A, together with multibeam dynamical Darwin model simulations,[55,56] as implemented in the software "xrayutilities".[57] This software has been used to retrieve the compositional profile of Figure 2f. A different piece of sample A has been further characterized by STEM and EDS. A JEOL Monochromated ARM200F TEM equipped with a monochromator, probe and image aberration correctors, and double silicon drift detector (SDD) EDS detectors was operated at 200 kV for STEM annular dark field (ADF) imaging and EDS analysis. The beam convergence semiangle used for STEM and EDS analysis was ∼27 mrad. The inner collection semiangle for ADF imaging was set to ∼55 mrad. The electron beam size was estimated to ∼1 Å in diameter. The STEM image (Figure 2c) shows ACQWs with sharp interfaces arranged in identical subsequent periods along the growth direction z.

IR Spectroscopy. A research-grade FTIR spectrometer (Bruker Vertex 70v) was used to collect the TM and TE transmission spectra, equipped with a wideband beamsplitter, a high linearity range MCT detector, a liquid-He flow optical cryostat (Janis Research co.) and a wire-grid lithographic KRS5 polarizer (Specac). The transmitted spectral intensity is measured for both TM and TE polarizations (electric field parallel and orthogonal to z, respectively). The dichroic absorption is calculated as $A = -\ln(\mathrm{TM}/\mathrm{TE})$, therefore, peaks correspond to z-dipole ISBTs and dip to xy-dipole ISBTs (one dip can be glimpsed at 42 THz in Figure 3c). The narrow $\gamma_{12} <$ 4 THz obtained at T = 10 K for all samples confirms the high quality of the heterostructures. At T = 10 K, only the fundamental subband 1 is populated, so the integrated spectral weight $\Sigma_I f_{1i}$ provides an estimate of the total hole sheet-density[38] in reasonable agreement with the nominal doping values (one has $N_1 \approx N_a$ see Table 1). The spectral weight ratios f_{13}/f_{12} = 0.96 and 0.82 for samples A and B, respectively, are reasonably close to unity, which represents the optimal value for SHG in ACQWs, as explained in ref 58, while we get f_{13}/f_{12} = 1.33 for the purposely detuned sample C.

For the first SHG experiment at 10 K, a monochromatic distributed feedback grating QCL (by Alpes Laser) emitting at λ = 10.3 μm, or ν_{QCL} = 29.3 THz ≈ $\nu_{13}/2$ was used to pump the SHG emission at T = 10 K, where ISBT line widths are narrowest. ZnSe lenses and wire-grid KRS5 polarizers were employed, together with the same optical cryostat of the FTIR setup. A MCT detector with a bandgap at λ = 8 μm was used to intrinsically reject the signal due to the pump photons, but thermal excitation of the detector by the pump beam could not be avoided. The resulting linear background was subtracted by offsetting the sample position along the optical axis (z-scan technique). The MCT detector and subsequent lock-in amplification chain was calibrated with a second QCL emitting at λ = 5.7 μm. The pump electric field was vertically polarized (TM), so only the tensor component $\chi^{(2)}_{zzz}$ was probed. The pump power was progressively attenuated from its maximum peak power P_{QCL} = 30 mW without varying the polarization

https://doi.org/10.1021/acsphotonics.1c01162
ACS Photonics XXXX, XXX, XXX–XXX

direction, using the cross-polarizer technique shown in Figure 4a (see Supporting Information, e). The collimated QCL beam was focused into the cryostat precisely at the center of the slab waveguide so as to maximize F_z in the ACQW layer.

For the second SHG experiment at 300 K, strong multicycle pump pulses were generated as described in,[50] centered at $\nu_{DFG,1}$ = 25 THz, $\nu_{DFG,2}$ = 29 THz or $\nu_{DFG,3}$ = 32 THz, and featuring a Fourier-transform-limited bandwidth $\Delta\nu_{DFG} \approx 2$ THz. The radiation exiting the waveguide was spectrally resolved with a mid-IR grating spectrometer in the range of 50−75 THz. Because $\Delta\nu_{DFG}$ values are narrower than the ISBT line widths at T = 300 K, they define the output SHG spectrum bandwidths equal to $2\Delta\nu_{DFG}$. Due to the high peak power density at focus up to 9×10^7 W/cm^2, the carrier temperature T_{holes} after optical pump absorption is expected to surpass the lattice temperature at 300 K, hence, making cryogenic cooling unessential.

All power values are estimated inside a generic sample, taking into account the reflection losses of 0.31 at the 20° Si-prism facet and, for the QCL experiment, the reflections at the KRS5 cryostat windows and polarizers.

■ ASSOCIATED CONTENT

Supporting Information

The Supporting Information is available free of charge at https://pubs.acs.org/doi/10.1021/acsphotonics.1c01162.

Additional theoretical calculations, experimental details, fitting results, and electron microscopy images of the samples (PDF)

■ AUTHOR INFORMATION

Corresponding Authors

Michele Virgilio − *Dipartimento di Fisica "E. Fermi", Università di Pisa, I-56127 Pisa, Italy*; Email: michele.virgilio@unipi.it

Michele Ortolani − *Dipartimento di Fisica, Sapienza Università di Roma, I-00185 Rome, Italy*; orcid.org/0000-0002-7203-5355; Email: michele.ortolani@roma1.infn.it

Authors

Jacopo Frigerio − *L-NESS, Dipartimento di Fisica, Politecnico di Milano, Polo di Como, I-22100 Como, Italy*

Chiara Ciano − *Dipartimento di Scienze, Università di Roma Tre, I-00146 Rome, Italy*

Joel Kuttruff − *Department of Physics and Center for Applied Photonics, University of Konstanz, D-78457 Konstanz, Germany*

Andrea Mancini − *Nanoinstitute Munich, Königinstrasse 10, Ludwig-Maximilians-Universität, D-80539 Munich, Germany; Dipartimento di Fisica, Sapienza Università di Roma, I-00185 Rome, Italy*; orcid.org/0000-0001-5927-9032

Andrea Ballabio − *L-NESS, Dipartimento di Fisica, Politecnico di Milano, Polo di Como, I-22100 Como, Italy*; orcid.org/0000-0002-2957-8717

Daniel Chrastina − *L-NESS, Dipartimento di Fisica, Politecnico di Milano, Polo di Como, I-22100 Como, Italy*

Virginia Falcone − *L-NESS, Dipartimento di Fisica, Politecnico di Milano, Polo di Como, I-22100 Como, Italy*

Monica De Seta − *Dipartimento di Scienze, Università di Roma Tre, I-00146 Rome, Italy*; orcid.org/0000-0002-8920-8371

Leonetta Baldassarre − *Dipartimento di Fisica, Sapienza Università di Roma, I-00185 Rome, Italy*; orcid.org/0000-0003-2217-0564

Jonas Allerbeck − *Department of Physics and Center for Applied Photonics, University of Konstanz, D-78457 Konstanz, Germany; Faculté des Sciences, de la Technologie et de la Communication, Université de Luxembourg, Luxembourg L-1511, Luxembourg*

Daniele Brida − *Faculté des Sciences, de la Technologie et de la Communication, Université de Luxembourg, Luxembourg L-1511, Luxembourg*

Lunjie Zeng − *Department of Physics, Chalmers University of Technology, 412 96 Gothenburg, Sweden*; orcid.org/0000-0002-4564-7217

Eva Olsson − *Department of Physics, Chalmers University of Technology, 412 96 Gothenburg, Sweden*; orcid.org/0000-0002-3791-9569

Complete contact information is available at: https://pubs.acs.org/10.1021/acsphotonics.1c01162

Author Contributions

‡These authors contributed equally to this work. The manuscript was written through contributions of all authors. All authors have given approval to the final version of the manuscript.

Funding

The research leading to these results has received funding from the Italian Ministry of Education, University, and Research (MIUR), PRIN Project ID 2017Z8TS5B. This project has received funding from the European Union's Horizon 2020 Research and Innovation Program under Grant Agreement Nos. 823717-ESTEEM3 and 766955-microSPIRE. This work has been supported by Fondazione Cariplo, Grant No. 2020−4427, by the LazioInnova project "TeraLaser", Grant No. A0375-2020-36579 and by Sapienza University of Rome, Grant No. PH11715C7E435F41.

Notes

The authors declare no competing financial interest.

■ ABBREVIATIONS

PIC,photonic integrated circuit; ACQW,asymmetric coupled quantum wells; SHG,second harmonic generation; ISBT,intersub-band transition; QCL,quantum cascade laser; DFG,difference frequency generation; FTIR,Fourier-transform IR spectroscopy; MCT,mercury−cadmium−telluride alloy; TM/TE,transverse magnetic/transverse electric

■ REFERENCES

(1) Zhang, L.; Agarwal, A. M.; Kimerling, L. C.; Michel, J. Nonlinear group IV photonics based on silicon and germanium: from near-infrared to mid-infrared. *Nanophotonics* **2014**, *3*, 247−268.

(2) Marris-Morini, D.; Vakarin, V.; Ramirez, J.-M.; Liu, Q.; Ballabio, A.; Frigerio, J.; Montesinos, M.; Alonso-Ramos, C.; Le Roux, X.; Serna, S.; Benedikovic, D.; Chrastina, D.; Vivien, L.; Isella, G. Germanium-based integrated photonics from near- to mid-infrared applications. *Nanophotonics* **2018**, *7*, 1781−1793.

(3) Borghi, M.; Castellan, C.; Signorini, S.; Trenti, A.; Pavesi, L. Nonlinear silicon photonics. *J. Opt.* **2017**, *19*, 093002.

(4) Lin, H.; Luo, Z.; Gu, T.; Kimerling, L. C.; Wada, K.; Agarwal, A.; Hu, J. Mid-infrared integrated photonics on silicon: a perspective. *Nanophotonics* **2017**, *7*, 393−420.
(5) Boyd, R. W. *Nonlinear Opt.*; Academic Press, 2002.
(6) Liu, S.; Keeler, G. A.; Reno, J. L.; Sinclair, M. B.; Brener, I. III−V Semiconductor nano-resonators-a new strategy for passive; active; and nonlinear all-dielectric metamaterials. *Adv. Opt. Mater.* **2016**, *4*, 1457−1462.
(7) Zhang, M.; Buscaino, B.; Wang, C.; Shams-Ansari, A.; Reimer, C.; Zhu, R.; Kahn, J. M.; Loncar, M. Broadband electro-optic frequency comb generation in a lithium niobate microring resonator. *Nature* **2019**, *568*, 373−377.
(8) Jones, D. J.; Diddams, S. A.; Ranka, J. K.; Stentz, A.; Windeler, R. S.; Hall, J. L.; Cundiff, S. T. Carrier-envelope phase control of femtosecond mode-locked lasers and direct optical frequency synthesis. *Science* **2000**, *288*, 635−639.
(9) Mosca, S.; Ricciardi, I.; Parisi, M.; Maddaloni, P.; Santamaria, L.; De Natale, P.; De Rosa, M. Direct generation of optical frequency combs in $\chi^{(2)}$ nonlinear cavities. *Nanophotonics* **2016**, *5*, 316−331.
(10) Absil, P. P.; Verheyen, P.; De Heyn, P.; Pantouvaki, M.; Lepage, G.; De Coster, J.; Van Campenhout, J. Silicon photonics integrated circuits: a manufacturing platform for high density; low power optical I/O's. *Opt. Express* **2015**, *23*, 9369.
(11) Lim, A. E-J.; Song, J.; Fang, Q.; Li, C.; Tu, X.; Duan, N.; Chen, K. K.; Tern, R. P.-C.; Liow, T. Y. Review of silicon photonics foundry efforts. *IEEE J. Sel. Top. Quantum Electron.* **2014**, *20*, 405−416.
(12) Franchi, R.; Castellan, C.; Ghulinyan, M.; Pavesi, L. Second-harmonic generation in periodically poled silicon waveguides with lateral p-i-n junctions. *Opt. Lett.* **2020**, *45*, 3188−3191.
(13) Ning, T.; Pietarinen, H.; Hyvarinen, O.; Simonen, J.; Genty, G.; Kauranen, M. Strong second-harmonic generation in silicon nitride films. *Appl. Phys. Lett.* **2012**, *100*, 161902.
(14) Lu, X.; Moille, G.; Rao, A.; Westly, D. A.; Srinivasan, K. Efficient photoinduced second-harmonic generation in silicon nitride photonics. *Nat. Photonics* **2021**, *15*, 131−136.
(15) Moss, D. J.; Morandotti, R.; Gaeta, A. L.; Lipson, M. New CMOS-compatible platforms based on silicon nitride and Hydex for nonlinear optics. *Nat. Photonics* **2013**, *7*, 597−607.
(16) Wang, C. Y.; Herr, T.; Del'Haye, P.; Schliesser, A.; Hofer, J.; Holzwarth, R.; Hansch, T. W.; Picque, N.; Kippenberg, T. J. Mid-infrared optical frequency combs at 2.5 μm based on crystalline microresonators. *Nat. Commun.* **2013**, *4*, 1345.
(17) Gaeta, A. L.; Lipson, M.; Kippenberg, T. J. Photonic-chip-based frequency combs. *Nat. Photonics* **2019**, *13*, 158−169.
(18) Makarov, S. V.; Petrov, M. I.; Zywietz, U.; Milichko, V.; Zuev, D.; Lopanitsyna, N.; Kuksin, A.; Mukhin, I.; Zograf, G.; Ubyivovk, E.; Smirnova, D. A.; Starikov, S.; Chichkov, B. N.; Kivshar, Y. S. Efficient Second-Harmonic Generation in Nanocrystalline Silicon Nanoparticles. *Nano Lett.* **2017**, *17*, 3047−3053.
(19) van Loon, M. A. W.; Stavrias, N.; Le, N. H.; Litvinenko, K. L.; Greenland, P. T.; Pidgeon, C. R.; Saeedi, K.; Redlich, B.; Aeppli, G.; Murdin, B. N. Giant multiphoton absorption for THz resonances in silicon hydrogenic donors. *Nat. Photonics* **2018**, *12*, 179.
(20) Le, N. H.; Lanskii, G. V.; Aeppli, G.; Murdin, B. N. Giant nonlinear susceptibility of hydrogenic donors in silicon and germanium. *Light: Sci. Appl.* **2019**, *8*, 64.
(21) Meng, F.; Thomson, M. D.; ul-Islam, Q.; Klug, B.; Pashkin, A.; Schneider, H.; Roskos, H. G. Intracavity third-harmonic generation in Si:B pumped by intense terahertz pulses. *Phys. Rev. B: Condens. Matter Mater. Phys.* **2020**, *102*, 075205.
(22) Fischer, M.; Riede, A.; Gallacher, K.; Frigerio, J.; Pellegrini, G.; Ortolani, M.; Paul, D. J.; Isella, G.; Leitenstorfer, A.; Biagioni, P.; Brida, D. Plasmonic mid-infrared third harmonic generation in germanium nanoantennas. *Light: Sci. Appl.* **2018**, *7*, 106.
(23) Rosencher, E.; Fiore, A.; Vinter, B.; Berger, V.; Bois, Ph; Nagle, J. Quantum engineering of optical nonlinearities. *Science* **1996**, *271*, 168−173.
(24) Sirtori, C.; Capasso, F.; Sivco, D. L.; Cho, A. Y. Nonlinear optics in coupled-quantum-well quasi-molecules. *Semiconductors and Semimetals*; Elsevier, 1999; Vol *66*, Ch. 2, pp 85−125.
(25) Vodopyanov, K. L.; O'Neill, K.; Serapiglia, G. B.; Phillips, C. C.; Hopkinson, M.; Vurgaftman, I.; Meyer, J. R. Phase-matched second harmonic generation in asymmetric double quantum wells. *Appl. Phys. Lett.* **1998**, *72*, 2654−2656.
(26) Lee, J.; Tymchenko, M.; Argyropoulos, C.; Chen, P.-Y.; Lu, F.; Demmerle, F.; Boehm, G.; Amann, M.-C.; Alu, A.; Belkin, M. A. Giant nonlinear response from plasmonic metasurfaces coupled to intersubband transitions. *Nature* **2014**, *511*, 65−69.
(27) Sarma, R.; De Ceglia, D.; Nookala, N.; Vincenti, M. A.; Campione, S.; Wolf, O.; Scalora, M.; Sinclair, M. B.; Belkin, A.; Brener, I. Broadband and efficient second-harmonic generation from a hybrid dielectric metasurface/semiconductor quantum-well structure. *ACS Photonics* **2019**, *6*, 1458−1465.
(28) Frigerio, J.; Ballabio, A.; Ortolani, M.; Virgilio, M. Modeling of second harmonic generation in hole-doped silicon-germanium quantum wells for mid-infrared sensing. *Opt. Express* **2018**, *26*, 31861−31872.
(29) Fischer, M. P.; Schmidt, C.; Sakat, E.; Stock, E.; Samarelli, A.; Frigerio, J.; Ortolani, M.; Paul, D. J.; Isella, G.; Leitenstorfer, A.; Biagioni, P.; Brida, D. Optical activation of germanium plasmonic antennas in the mid-infrared. *Phys. Rev. Lett.* **2016**, *117*, 047401.
(30) Seto, M.; Helm, M.; Moussa, Z.; Boucaud, P.; Julien, F. H.; Lourtioz, J.-M.; Nützel, J. F.; Abstreiter, G. Second-harmonic generation in asymmetric Si/SiGe quantum wells. *Appl. Phys. Lett.* **1994**, *65*, 2969−2971.
(31) Grimm, C. V.-B.; Priegnitz, M.; Winnerl, S.; Schneider, H.; Helm, M.; Biermann, K.; Künzel, H. Intersubband relaxation dynamics in single and double quantum wells based on strained InGaAs/AlAs/AlAsSb. *Appl. Phys. Lett.* **2007**, *91*, 191121.
(32) Qian, H.; Li, S.; Chen, C. F.; Hsu, S. W.; Bopp, S. E.; Ma, Q.; Tao, A. R.; Liu, Z. Large optical nonlinearity enabled by coupled metallic quantum wells. *Light: Sci. Appl.* **2019**, *8*, 13.
(33) Wolf, O.; Campione, S.; Benz, A.; Ravikumar, A. P.; Liu, S.; Luk, T. S.; Kadlec, E. A.; Shaner, E. A.; Klem, J. F.; Sinclair, M. B.; Brener, I. Phased-array sources based on nonlinear metamaterial nanocavities. *Nat. Commun.* **2015**, *6*, 7667.
(34) Chaisakul, P.; Marris-Morini, D.; Frigerio, J.; Chrastina, D.; Rouifed, M.-S.; Cecchi, S.; Crozat, P.; Isella, G.; Vivien, L. Integrated germanium optical interconnects on silicon substrates. *Nat. Photonics* **2014**, *8*, 482−488.
(35) Kuo, Y.-H.; Lee, Y. K.; Ge, Y.; Ren, S.; Roth, J. E.; Kamins, T. I.; Miller, D. A. B.; Harris, J. S. Strong quantum confined Stark effect in germanium quantum-well structures on silicon. *Nature* **2005**, *437*, 1334−1336.
(36) Lever, L.; Hu, Y.; Myronov, M.; Liu, X.; Owens, N.; Gardes, F. Y.; Marko, S. J.; Sweeney, S. J.; Ikonic, Z.; Leadley, D. R.; Reed, G. T.; Kelsall, R. W. Modulation of the absorption coefficient at 1.3 mm in Ge/SiGe multiple quantum well heterostructures on silicon. *Opt. Lett.* **2011**, *36*, 4158−4160.
(37) Grange, T.; Stark, D.; Scalari, G.; Faist, J.; Persichetti, L.; Di Gaspare, L.; De Seta, M.; Ortolani, M.; Paul, D. J.; Capellini, G.; Birner, S.; Virgilio, M. Room temperature operation of n-type Ge/SiGe terahertz quantum cascade lasers predicted by non-equilibrium Green's functions. *Appl. Phys. Lett.* **2019**, *114*, 111102.
(38) Ciano, C.; Virgilio, M.; Montanari, M.; Persichetti, L.; Di Gaspare, L.; Ortolani, M.; Baldassarre, L.; Zoellner, M.H.; Skibitzki, O.; Scalari, G.; Faist, J.; Paul, D.J.; Scuderi, M.; Nicotra, G.; Grange, T.; Birner, S.; Capellini, G.; De Seta, M. Control of electron-state coupling in asymmetric Ge/Si−Ge quantum wells. *Phys. Rev. Appl.* **2019**, *11*, 014003.
(39) Chang, Y.-C.; Paeder, V.; Hvozdara, L.; Hartmann, J.-M.; Herzig, H. P. Low-loss germanium strip waveguides on silicon for the mid-infrared. *Opt. Lett.* **2012**, *37*, 2883−2885.
(40) Brun, M.; Labeye, P.; Grand, G.; Hartmann, J.-M.; Boulila, F.; Carras, M.; Nicoletti, S. Low loss SiGe graded index waveguides for mid-IR applications. *Opt. Express* **2014**, *22*, 508−518.

https://doi.org/10.1021/acsphotonics.1c01162
ACS Photonics XXXX, XXX, XXX−XXX

(41) Nedeljkovic, M.; Penades, J. S.; Mittal, V.; Murugan, S. M.; Khokhar, A. Z.; Littlejohns, C.; Carpenter, L. G.; Gawith, C. B. E.; Wilkinson, J. S.; Mashanovich, G. Z. Germanium-on-silicon waveguides operating at mid-infrared wavelengths up to 8.5 μm. *Opt. Express* **2017**, *25*, 27431−27441.
(42) Ramirez, J. M.; Liu, Q.; Vakarin, V.; Frigerio, J.; Ballabio, A.; Le Roux, X.; Bouville, D.; Vivien, L.; Isella, G.; Marris-Morini, D. Graded SiGe waveguides with broadband low-loss propagation in the mid infrared. *Opt. Express* **2018**, *26*, 870−877.
(43) Gallacher, K.; Millar, R. W.; Griškevičiūte, U.; Baldassarre, L.; Sorel, M.; Ortolani, M.; Paul, D. J. Low loss Ge-on-Si waveguides operating in the 8−14 μm atmospheric transmission window. *Opt. Express* **2018**, *26*, 25667−25675.
(44) Gallacher, K.; Millar, R. W.; Paul, D. J.; Frigerio, J.; Ballabio, A.; Isella, G.; Rusconi, F.; Biagioni, P.; Giliberti, V.; Sorgi, A.; Baldassarre, L.; Ortolani, M. Characterization of integrated waveguides by atomic-force-microscopy-assisted mid-infrared imaging and spectroscopy. *Opt. Express* **2020**, *28*, 22186−22199.
(45) Gallacher, K.; Millar, R. W.; Griškevičiūte, U.; Sinclair, M.; Sorel, M.; Baldassarre, L.; Ortolani, M.; Soref, R.; Paul, D. J. Ultra-broadband mid-infrared Ge-on-Si waveguide polarization rotator. *APL Photonics* **2020**, *5*, 026102.
(46) Li, S.; Khurgin, J. Second-order nonlinear optical susceptibility in p-doped asymmetric quantum wells. *Appl. Phys. Lett.* **1993**, *62*, 1727−1729.
(47) Isella, G.; Chrastina, D.; Rossner, B.; Hackbarth, T.; Herzog, H. J.; Konig, U.; Von Kanel, H. Low-energy plasma-enhanced chemical vapor deposition for strained Si and Ge heterostructures and devices. *Solid-State Electron.* **2004**, *48*, 1317−1323.
(48) Bashir, A.; Gallacher, K.; Millar, R. W.; Paul, D. J.; Ballabio, A.; Frigerio, J.; Isella, G.; Kriegner, D.; Ortolani, M.; Barthel, J.; MacLaren, I. Interfacial sharpness and intermixing in a Ge-SiGe multiple quantum well structure. *J. Appl. Phys.* **2018**, *123*, 035703.
(49) Cecchi, S.; Gatti, E.; Chrastina, D.; Frigerio, J.; Mueller-Gubler, E.; Paul, D. J.; Guzzi, M.; Isella, G. Thin SiGe virtual substrates for Ge heterostructures integration on silicon. *J. Appl. Phys.* **2014**, *115*, 093502.
(50) Grupp, A.; Budweg, A.; Fischer, M. P.; Allerbeck, J.; Soavi, G.; Leitenstorfer, A.; Brida, D. Broadly tunable ultrafast pump-probe system operating at multi-kHz repetition rate. *J. Opt.* **2018**, *20*, 014005.
(51) Virgilio, M.; Grosso, G. Valence and conduction intersubband transitions in SiGe; Ge-rich; quantum wells on [001] Si0.5Ge0.5 substrates: A tight-binding approach. *J. Appl. Phys.* **2006**, *100*, 093506.
(52) Virgilio, M.; Grosso, G. Valley splitting and optical intersubband transitions at parallel and normal incidence in [001]-Ge/SiGe quantum wells. *Phys. Rev. B: Condens. Matter Mater. Phys.* **2009**, *79*, 165310.
(53) Jancu, J.-M.; Scholz, R.; Beltram, F.; Bassani, F. Empirical spds* tight-binding calculation for cubic semiconductors: General method and material parameters. *Phys. Rev. B: Condens. Matter Mater. Phys.* **1998**, *57*, 6493−6507.
(54) Jancu, J.-M.; Voisin, P. Tetragonal and trigonal deformations in zinc-blende semiconductors: A tight-binding point of view. *Phys. Rev. B: Condens. Matter Mater. Phys.* **2007**, *76*, 115202.
(55) Morelhão, S. L.; Fornari, C. I.; Rappl, P. H. O.; Abramof, E. Nanoscale characterization of bismuth telluride epitaxial layers by advanced X-ray analysis. *J. Appl. Crystallogr.* **2017**, *50*, 399−410.
(56) Darwin, C. G. The theory of X-ray reflection. *Philos. Mag.* **1914**, *27*, 315−333.
(57) Kriegner, D.; Wintersberger, E.; Stangl, J. Xrayutilities: a versatile tool for reciprocal space conversion of scattering data recorded with linear and area detectors. *J. Appl. Crystallogr.* **2013**, *46*, 1162−1170.
(58) Vurgaftman, I.; Meyer, J. R. L.; Ram-Mohan, R. Optimized second-harmonic generation in asymmetric double quantum wells. *IEEE J. Quantum Electron.* **1996**, *32*, 1334−1346.

https://doi.org/10.1021/acsphotonics.1c01162
ACS Photonics XXXX, XXX, XXX−XXX